

Transient slip events from near-field seismic and geodetic data on a glacier fault, Whillans Ice Plain, West Antarctica

Jacob I. Walter,¹ Emily E. Brodsky,¹ Slawek Tulaczyk,¹ Susan Y. Schwartz,¹ and Rickard Pettersson²

Received 26 April 2010; revised 22 November 2010; accepted 21 December 2010; published 11 March 2011.

[1] Bidaily, tidally modulated stick-slip speed-ups of the Whillans Ice Plain (WIP) provide insight into glacier dynamics and failure at a naturally repeating fault asperity. We installed a network of continuously operating GPS receivers in 2007 and deployed on-ice broadband seismometers during the austral summer of 2008 on Whillans Ice Stream (WIS), West Antarctica, and recorded 26 glacier speed-up events. Previous work during the 2004 field season suggested that these speed-ups initiate as failure of an asperity on or near “ice raft A” that triggers rupture across the entire WIP. Our results for 2008 locate the slip initiation farther to the south of this feature, closer to the grounding line and the southernmost extent of the Ross Ice Shelf. The initiation may be controlled by a discontinuity in basal boundary conditions at the suture between two ice streams. A strong correlation between the amplitude of seismic waves generated at the rupture front and the total slip achieved over the duration of the slip event (~30 min) suggests slip-predictable behavior, i.e., the ability to forecast the eventual slip based on the first minute of seismic radiation. Successive slip events propagate with different rupture speeds (100–300 m/s) that strongly correlate ($R^2 = 0.73$) with the interevent duration. In addition, the amount of slip achieved during each event appears to be correlated with the rupture speed. We use these observations to constrain basal shear stress to be 4 kPa by calculating conditions for basal freezing. Our observations yield information regarding mechanics and dynamics of ice streambeds at the scale of tens to hundreds of kilometers. Subglacial processes are notoriously difficult to constrain on these large scales, which are relevant to the understanding of regional and continental ice motion.

Citation: Walter, J. I., E. E. Brodsky, S. Tulaczyk, S. Y. Schwartz, and R. Pettersson (2011), Transient slip events from near-field seismic and geodetic data on a glacier fault, Whillans Ice Plain, West Antarctica, *J. Geophys. Res.*, 116, F01021, doi:10.1029/2010JF001754.

1. Introduction

[2] The recently discovered episodic slip events on the Whillans Ice Stream in Antarctica indicate that twice a day the glacier locally speeds up to a slip rate of tens of centimeters per hour for 20–30 min periods [Bindschadler *et al.*, 2003a]. Wiens *et al.* [2008] have shown that the slip velocity of the ice becomes fast enough during these slip events to generate seismic waves that are observable at far-field stations near the South Pole (QSPA) and the Dry Valleys, Antarctica (VNDA).

[3] Twice daily stick slips are intrinsically interesting as a direct indication of the mode of glacier motion and episodic slip provides a window into the physical conditions at the base of the glacier. Periodic or episodic movement in a

system driven by far-field, steady motion is a hallmark of stick slip as most commonly evidenced by earthquakes on tectonic faults [e.g., Brace and Byerlee, 1966]. Winberry *et al.* [2009] suggest that this basic stick-slip model is applicable to the ice sheet, where the base is locked by friction between events and loaded by elastic strain accumulation in the glacier. Eventually the local frictional resistance is overcome and the glacier jerks forward, releasing the elastic stress, and beginning the cycle again. In this scenario, the timing, size, and location of the slip events provide information about the basal friction, and its control on overall glacial movement.

[4] In this paper, we use newly acquired field data and techniques borrowed from the tectonic earthquake community to closely study these episodic slip events, to constrain the conditions at the base of the glacier. After describing the data collection, we highlight five key observations about glacial slip events: (1) the presence and shape of an initiation phase in addition to previously reported stopping phases, (2) the variability of the rupture speed and its association with final slip, (3) the location of the start of slip events,

¹Department of Earth and Planetary Sciences, University of California, Santa Cruz, California, USA.

²Department of Earth Sciences, Uppsala University, Uppsala, Sweden.

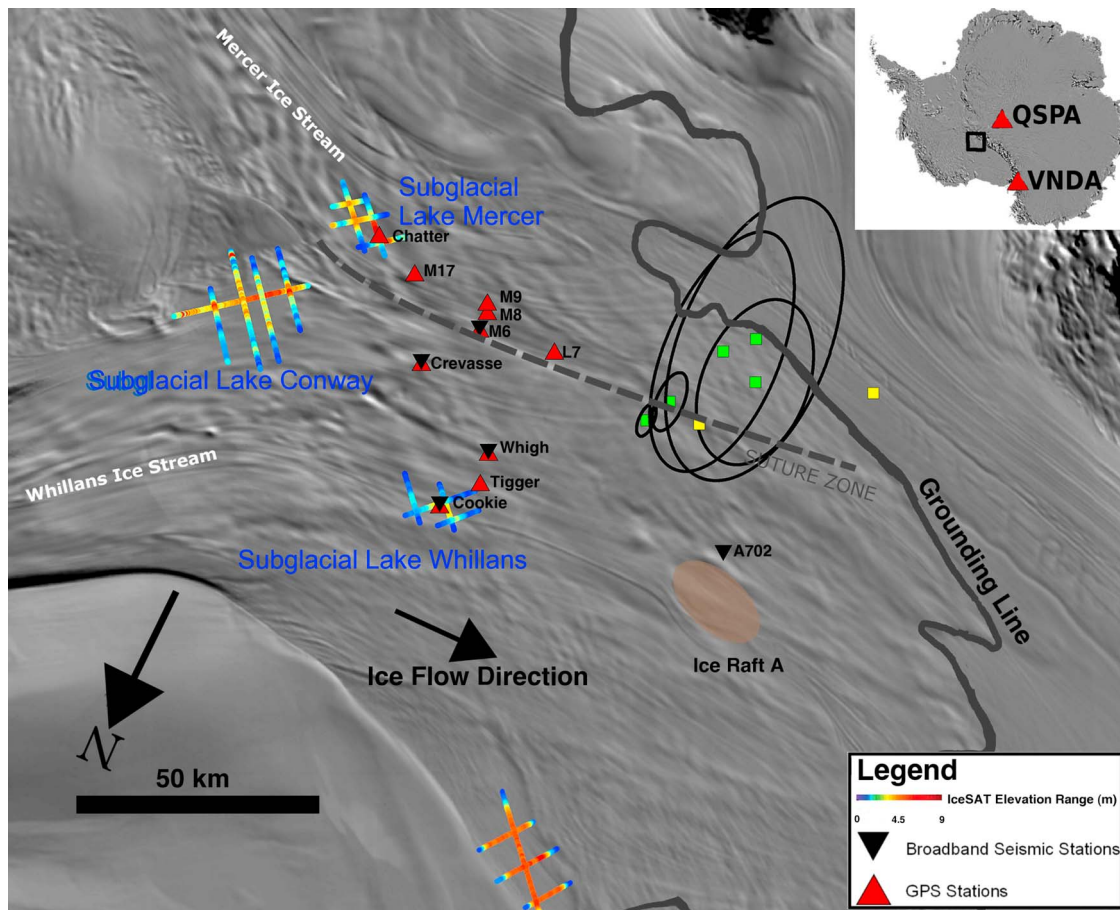


Figure 1. Station location map depicting continuous GPS network and broadband station names for the 2008 field season. Subglacial lake geometry is shown as IceSAT tracks [Fricker *et al.*, 2007]. Grounding line is shown, adapted from Horgan and Anandakrishnan [2006]. The circles are 95% confidence level error ellipses encircling slip start locations, shown as green squares. Yellow squares indicate slip start locations with only three station observations; others have at least four observations. The suture zone location is based on the presence of buried crevasses detected by airborne radar sounding [Shabtaie *et al.*, 1987]. The suture zone is the boundary between Mercer- and Whillans-sourced ice.

(4) the correlation between the initiation phase amplitude and the final slip, and (5) the presence of interevent stable sliding. We then proceed to combine and interpret these observations to address five different physical points: (1) the relationship between glacial slip and tectonic earthquakes, (2) the physical controls on the start of slip, (3) the slip predictability, (4) the stress drop during events, and (5) the role of basal freezing in healing.

2. Data Collection

2.1. Seismic and Geodetic Data

[5] During December of 2007, we established a network of continuously sampling GPS stations on WIS/WIP at strategic locations to capture the hydrology and dynamics of an active subglacial lake network [Fricker *et al.*, 2007]. We used the online precise point positioning (PPP) service provided by Natural Resources Canada (http://www.geod.nrcan.gc.ca/online_data_e.php) to obtain a position for each sample. The GPS receivers record a position every 15 s and

have operated continuously since installation, with plans to operate through 2014.

[6] Following the establishment of the GPS network, in the November/December 2008 field season, we operated broadband seismometers on WIS. The broadband seismometers operated at 100 Hz and all but one (A702) were collocated with continuous GPS stations (Figure 1). In addition, we used far-field data from the Global Seismic Network (GSN), including stations QSPA and VNDA, which are about 650 and 990 km away, respectively, from WIP. Their location relative to our field study area appears on Figure 1.

2.2. Ice-Penetrating Radar

[7] Context for the slip events is provided by data on the subglacial structure from ice-penetrating radar. In a previous field season (November 2007), we collected about 180 km of radar profiles in a transect crossing the suture zone, where the WIS and Mercer Ice Stream (MIS) converge to form the Whillans Ice Plain (WIP). The transect crosses through GPS

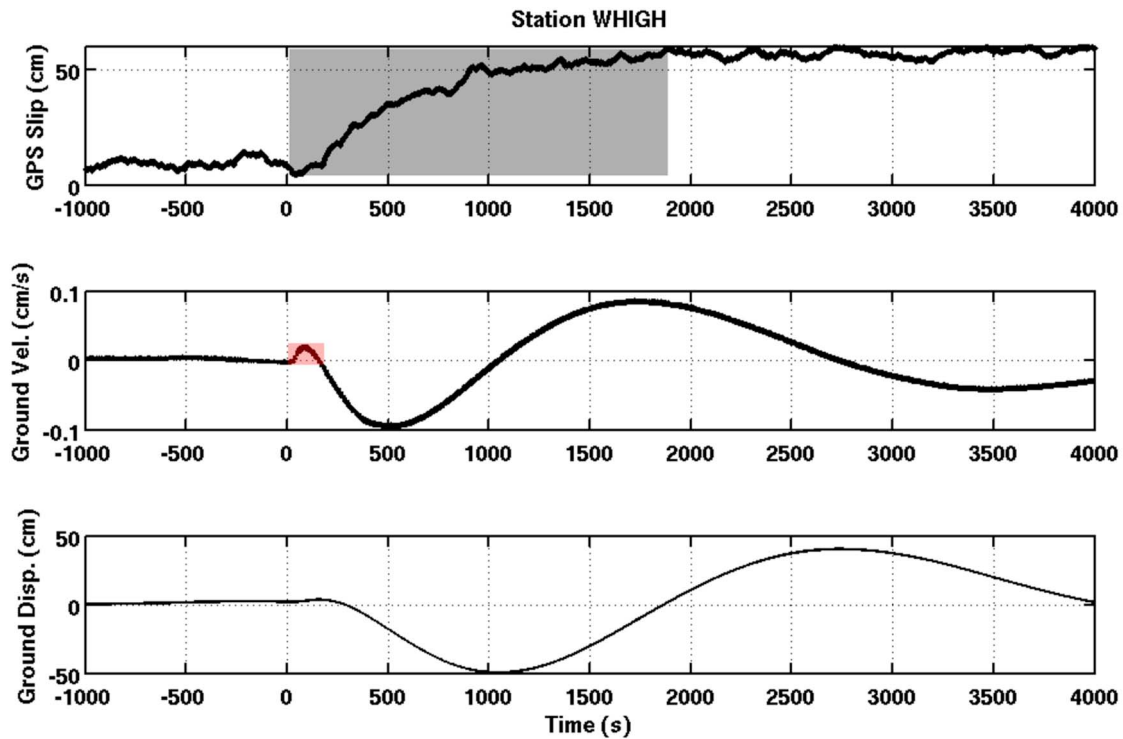


Figure 2. (top) GPS displacement, (middle) seismic ground velocity, and (bottom) seismic displacement on the east component at a collocated site. Seismic data has been high-pass filtered at 3000 s (0.0003 Hz). Red box indicates the medium-period slip initiation pulse, and the gray box encapsulates the total slip and duration of the slip event. Note the comparable displacement amplitudes for the (top) GPS and (bottom) seismic. The seismic displacement amplitude is negative near ~ 1000 s because the slip direction is predominantly west.

stations M6, M8, and M9, and continues along this general line southwest. The radar data were collected using a ground-based low-frequency impulse radar with 10 MHz resistively loaded dipole antennas, giving a pulse wavelength of ~ 20 m in ice. The transmitter consisted of a solid state high-voltage pulse source with a repetition frequency of 1 kHz. The receiver was a 12-bit low-noise digitizer. Individual traces were stacked 200 times and the average trace spacing was 18 m. Trace locations were determined using geodetic two-frequency GPS measurements. The collected data were corrected for normal moveout, dewowed, and low-pass filtered before being displayed. Conversion of travel times to depth was done assuming a wave speed in ice of 168 m/s.

[8] Relative reflectivity of the bed was estimated using the method of *Jacobel et al.* [2009] who use recorded returned power of the bed as a proxy for bed conditions, where stronger bed returns are typically interpreted as wetter bed. The method requires that the recorded bed power is corrected for geometrical spreading, as well as, attenuation in the ice column. The geometrical spreading can be easily corrected for, but the attenuation within the ice is more difficult to estimate. A common approach in radioglaciology is to use spatial variations in bed power normalized to a constant depth as a proxy for englacial attenuation [*Gades et al.*, 2000; *Winebrenner et al.*, 2003; *Jacobel et al.*, 2009]. In this study we use the variations in depth-averaged returned

bed power from all our profiles to estimate the attenuation rate. This gives an attenuation rate of 23.7 dB/km, which is similar to earlier reported attenuation rates for ice streams in West Antarctica [*Jacobel et al.*, 2009, and references therein]. After correcting for geometric spreading and englacial attenuation, the returned bed power is assumed to depend mainly on the dielectric contrast across the ice-bed interface and is taken to be a proxy for the water abundance at the bed.

3. Observations

3.1. Slip Event Description

3.1.1. Near-Field Records of Slip Events

[9] We recorded a series of slip events at the on-ice, collocated continuous GPS receivers and broadband seismometers. Slip events typically last 25–30 min and have total displacements of 0.2–0.5 m (Figure 2). At each locale, the onset of slip is rapid, as revealed by the steep slope of the GPS records. The collocated seismometers record a small amplitude, medium period (< 100 s) arrival coincident with the GPS slip onset (red box in middle panel of Figure 2). We will refer to this portion of the wave as the initiation phase throughout the remainder of the paper. After the initiation phase, the seismograms record the same integrated displacement as the GPS records, as the instruments move along with the slipping ice (Figure 2, bottom).

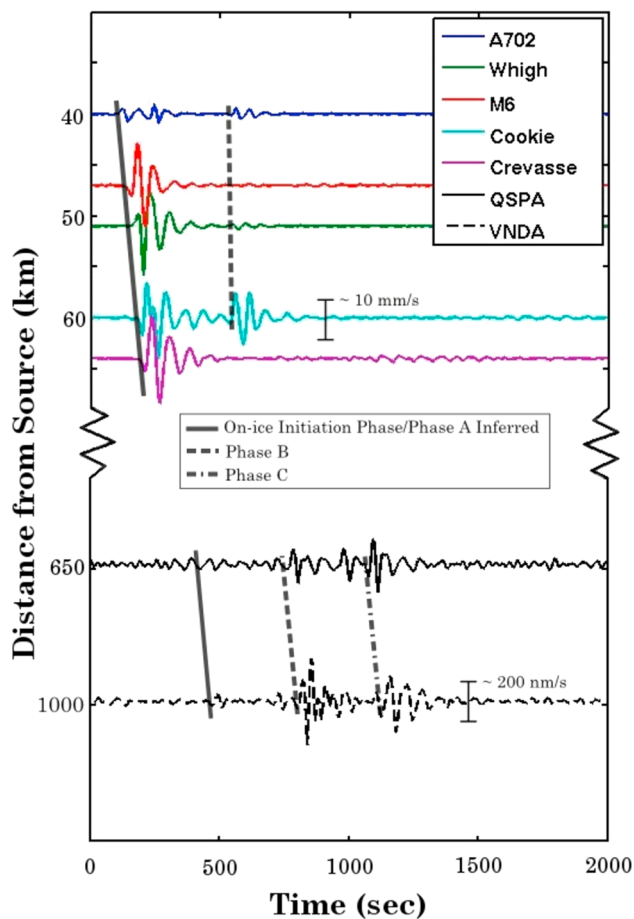


Figure 3. Seismic record section of a single event observed at both on-ice and far-field stations. At the on-ice stations, the initiation phase (solid gray line through color stations) indicates the rupture front propagating across the Ice Plain and its modeled arrival at far-field stations (most events in 2008 do not transmit sufficient phase A energy to be detectable above the noise). On-ice, the initiation phase is the seismic energy associated with the passing rupture front (maximum ~ 0.3 km/s) observed at each individual station. In the far field, phase A is a seismic wave (~ 3 km/s) associated with the slip start, which is a distance away from the on-ice stations. A diagram of the rupture process is also found on Figure 4.

[10] The seismic initiation phase arrives synchronous with the start of GPS slip for every slip event and is recorded on each station as the rupture front sweeps across the network (Figure 3). In the record section shown on Figure 3, the seismic data have been band passed (0.012–0.04 Hz) in order to highlight the energy contained within the initiation phase.

[11] In addition to recording the initiation of the slip events as the rupture front passes beneath each station, some of the on-ice stations also record evidence of the rupture front stopping at a discrete location ~ 100 km from its origin. Figure 3 depicts this stopping phase, which we call phase B, as observed in the near-field records. Far-field seismic records show at least two stopping phases, and we describe these in more detail in section 3.1.2.

3.1.2. Far-Field Records of Slip Events

[12] We obtained broadband seismic data from far-field stations VNDA (~ 990 km from WIP) and QSPA (~ 650 km from WIP) for the time period overlapping operation of our on-ice stations. Examples of waveforms from these stations appear on the bottom half of Figure 3. Figure 3 contains a case of a triple-phase long-period waveform from VNDA first described by *Wiens et al.* [2008]. Throughout this paper, we refer to the three phases on the far-field record as phase A, phase B, and phase C (Figure 3). Of the 26 slip events observed during our 2008 field season, only 5 had all three phases (A, B, and C) visible on VNDA records, with the majority lacking phase A (record sections for all of the slip events are included in Text S2 of the auxiliary material).¹ Phase B is visible on VNDA records for 22 of 26 events and phase C is visible on VNDA records for 17 of 26 events.

[13] *Wiens et al.* [2008] suggested that the triple-phased long-period waveforms visible at stations VNDA and QSPA are Rayleigh waves representing a starting and two stopping phases of the WIP slip (Figure 4). They located the initiation of the slips (phase A) at “ice raft A,” whose outline appears on Figure 1, using a grid search of the GPS slip initiation. Phase B and C arrivals were interpreted to be stopping phases and located both using a surface wave grid search technique. According to their methods, phase B locates ~ 50 km south of ice raft A, near the region we suggest the slips start, and phase C locates ~ 120 km north of ice raft A.

[14] Phase B arrives at VNDA ~ 11 – 24 min after the first detected motion on the Ice Plain. The travel time for a Rayleigh wave originating at the Ice Plain would be only ~ 5.5 min. In section 3.2, we show that this can be explained by a rupture speed variation of up to a factor of two between subsequent events. When phase B is generated, the on-ice stations (A702 and Cookie) consistently observe phase B ~ 5.5 min prior to VNDA. The constant relative timing of the near-field and far-field arrival supports their identification as the same seismic phase.

[15] The on-ice stations never record phase A. If this phase corresponds to the initiation of rupture at the origin of the slip event as proposed by *Wiens et al.* [2008], then it originates ~ 50 km from any of our stations (A more precise location will be provided in section 3.3). Absence of phase A arrivals in the near-field records suggests that it does not propagate in ice at close distances. Phase A is distinct from the initiation phase that accompanies the beginning of slip at each station. Phase A records the global initiation of slip on the ice stream; the initiation phase records the local slip start as the rupture front arrives at a station.

3.2. Rupture Speed Variations

[16] The difference in time between the arrival of stopping phase B at station VNDA and the start of a slip event detected at on-ice stations varies between events. The difference covers a range of ~ 11 – 24 min, which is much greater than the ~ 5.5 min travel time for a Rayleigh wave originating at WIS to travel ~ 1000 km to VNDA. The range in the arrival time of phase B suggests that the time for the slip

¹Auxiliary materials are available in the HTML. doi:10.1029/2010JF001754.

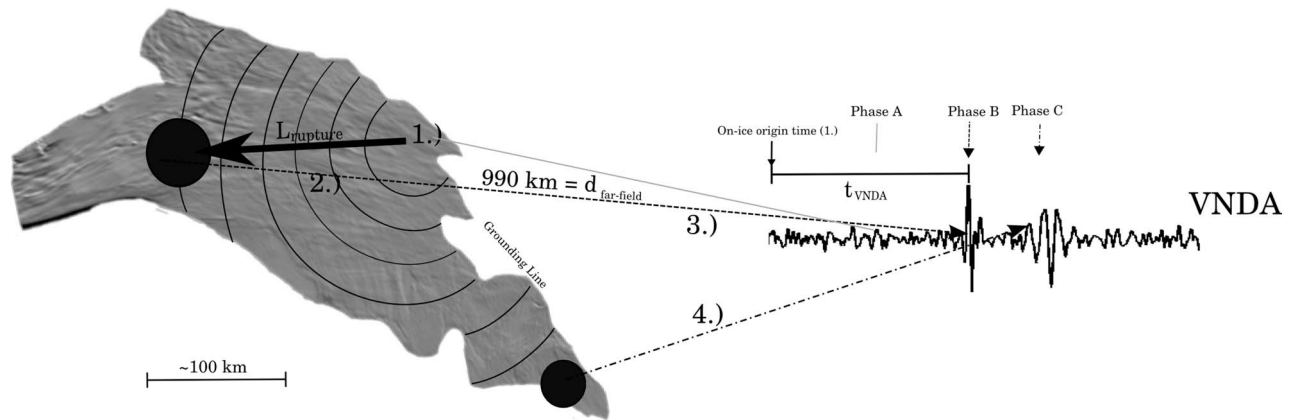


Figure 4. Schematic of method for far-field inference of rupture speed. (1) Rupture initiates at a location adjacent to the grounding line, (2) propagates across the ice at a rupture speed determined by equation (1), (3) the rupture stops spreading at one stopping point which transmits phase B of the far-field wave, (4) the rupture stops at another stopping point and transmits phase C of the far-field wave. The origin time is inferred from the seismic initiation phase at the on-ice stations. The origins of phases B and C are not constrained and only shown schematically phase A is weak or unobservable on the example seismogram and the expected arrival time is shown for clarity.

to rupture across the WIP varies from ~ 5 – 18 min. Such a range in rupture time can be generated by subsequent changes in either rupture speed or rupture length. Previous work [Wiens *et al.*, 2008] showed that the rupture speed varies from 0.1 to 0.2 km/s for each event. Therefore, we first investigate the possibility that the range of phase B arrivals is due entirely to variation in rupture velocity. Later, we will pursue the alternative hypothesis by varying the rupture length.

[17] The total travel time observed for phase B is the sum of the on-ice rupture time and the propagation time from the arrest location to the station (Figure 4). Assuming that the wave travels from the Ice Plain to the station as a Rayleigh wave, the propagation time can be calculated. Therefore, if we assume a constant rupture length, we calculate a rupture velocity from the observed travel times. The rupture velocity in this model is

$$V_{\text{rupture}} = \frac{L_{\text{rupture}}}{t_{\text{VNDA}} - \frac{d_{\text{far-field}}}{V_{\text{Rayleigh}}}}, \quad (1)$$

where V_{Rayleigh} is the Rayleigh wave speed (3 km/s), $d_{\text{far-field}}$ is the distance to the station, L_{rupture} is the length of rupture, and t_{VNDA} is the difference in time between the origin time and arrival of phase B at station VNDA (Figure 4). We use values of 990 km and 100 km for $d_{\text{far-field}}$ and L_{rupture} , respectively. Both of these values are approximate. Based on the configuration in Figure 1, the far-field distance can vary by about 100 km. This uncertainty results in ~ 30 s uncertainty in travel time, which is at maximum $< 5\%$ of the observed arrival time variability. The inferred rupture velocities are more strongly dependent on L_{rupture} and this sensitivity will be explored below. We use VNDA arrivals, rather than QSPA, for rupture speed analysis, as they are detected more frequently.

[18] Typical values for rupture speed based on equation (1) vary between 0.1 and 0.3 km/s (Table S2 in Text S1 of the auxiliary material). This range is comparable to the range of previous work on WIP slip events and significantly below the usual rupture speed for earthquakes (~ 3 km/s) [e.g., Kanamori and Brodsky, 2004].

[19] We now consider the alternative hypothesis that rupture length variability controls the variability in phase B arrival times. Because our GPS network is not able to observe the entirety of the rupture area, we do not have direct constraints on L_{rupture} . We therefore calculate values of L_{rupture} from equation (1) with fixed rupture speeds and the observed arrival times and evaluate the plausibility of the resulting values. The minimum value of $V_{\text{rupture}} = 0.1$ km/s corresponds to inferred rupture lengths of 38–78 km and the maximum of $V_{\text{rupture}} = 0.3$ km/s results in 95–234 km. The length of 234 km exceeds any dimension of the WIP and 38–78 km is smaller than the distance between many of the stations and the furthest slip start location. The rupture speed fluctuations therefore provide the more plausible cause of the large range (~ 11 – 24 min) of arrival time variations at the far-field station.

[20] A closer look at the phase B and C separation also provides important constraints upon the varying nature of the rupture speeds. In order to assess phase and/or amplitude variations between subsequent events, we plot various waveforms for VNDA with respect to each rupture velocity as inferred from equation (1) on Figure 5a. Figure 5a shows that the lag between phase B and phase C arrivals increases with decreasing rupture velocity. This suggests that phase B and C, as stopping phases, have fixed locations, a feature also identified by Wiens *et al.* [2008]. Multiplying the time difference between the phase B and phase C arrivals at the maximum and minimum rupture speeds, yields a consistent value of ~ 60 km. This value is a minimum rupture distance perpendicular to the wavefront from the initiation point, for the two stopping locations.

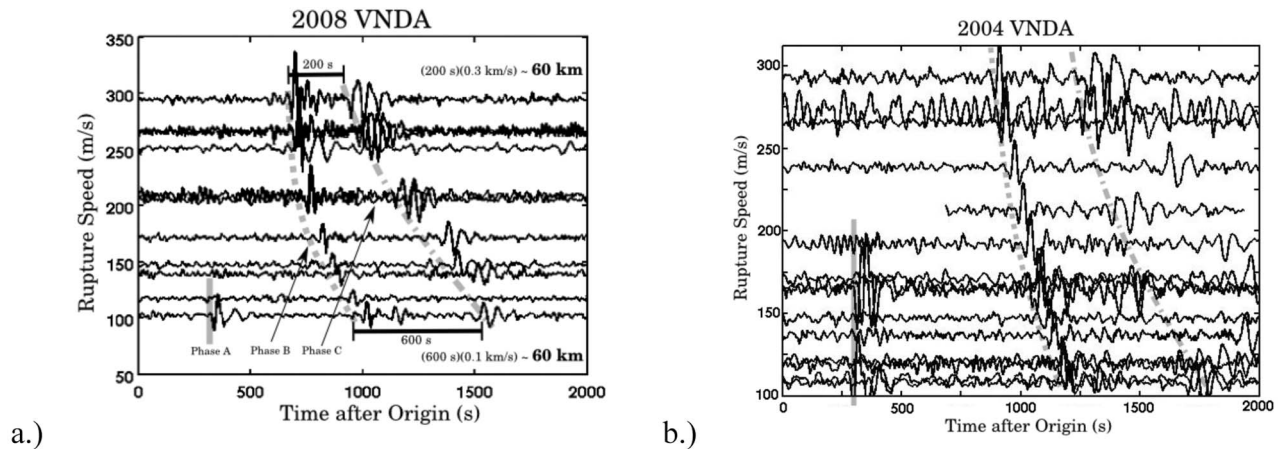


Figure 5. Waveforms of a suite of slip events observed at station Vnda in (a) 2008 and (b) 2004, plotted as a function of rupture speed. The waveforms are adjusted so that the origin (time = 0) corresponds to the on-ice origin time. If phase A were visible at station Vnda for all events, that arrival time would be near the 350 s mark. The time difference between phase B and phase C arrivals varies linearly with rupture speed, such that an estimated distance of 60 km separates the physical locations of phase B and phase C decelerating points.

[21] A similar pattern is seen for data from 2004. *Wiens et al.* [2008] published a catalog of slip event origin times for their field season in the austral summer of 2004. We obtained Vnda data for 2004 and with use of the *Wiens et al.* [2008] catalog, we repeated the steps described above and obtained rupture velocity estimates consistent with our observations in 2008 (Figure 5b). Although the basic pattern of arrivals is the same, there is one clear difference. The 2004 data contain more phase A arrivals than are present for slip events in 2008. In both 2004 and 2008, the slip events with lower rupture velocities seem to preferentially generate phase A arrivals.

[22] Another distinguishing feature of these slip events is that the total slip achieved over the slip event scales with the rupture velocity. Figure 6 indicates a strong correlation (R^2 value of 0.79 and p value of 0.0005) between the GPS slip and inferred rupture velocity. Previous work hinted at the possibility of such a correlation, as *Wiens et al.* [2008] qualitatively observed a correlation between Ross Sea tidal amplitude and rupture velocity, and *Winberry et al.* [2009] modeled the stress balance on the WIP from ocean tides showing that high tide increases shear stress, which corresponds to increased slip. Therefore, the correlation between rupture velocity and slip was implicit in the earlier work, but was not specifically addressed until now.

3.3. Location of Slip Start

[23] We locate the start of the slip events by inverting the initiation phase arrival times for the on-ice seismometers from the 2008 field season (Figure 1). We implement a 2-D (x, y, t) linear least squares inversion of the arrival times by assuming a unique rupture speed for each event (see Appendix A for a detailed description). The rupture speed varies between events and an average quantity is inferred from equation (1) for each individual event. We also calculate error ellipses, with two standard deviations representing the 95% confidence interval (Figure 1). The zone encompassed

by our locations and error ellipses is south of our seismic network and adjacent to the grounding line.

[24] Seismic arrival times are much more reliable for timing of the rupture front propagation than determining arrival of the rupture using GPS, as it is difficult to accurately pick an arrival time on coarsely sampled GPS data (15s sample spacing in this study). At colocated stations, automatic and handpicked GPS initiation times can range from simultaneous to 60 s after the seismic arrival. Therefore, picking seismic arrivals is better suited for inverting for the origin of the slip start.

[25] The zone does not intersect ice raft A, as suggested by *Wiens et al.* [2008]. One possible issue is that *Wiens et al.* [2008] state that the rupture speed is ~ 1000 m/s

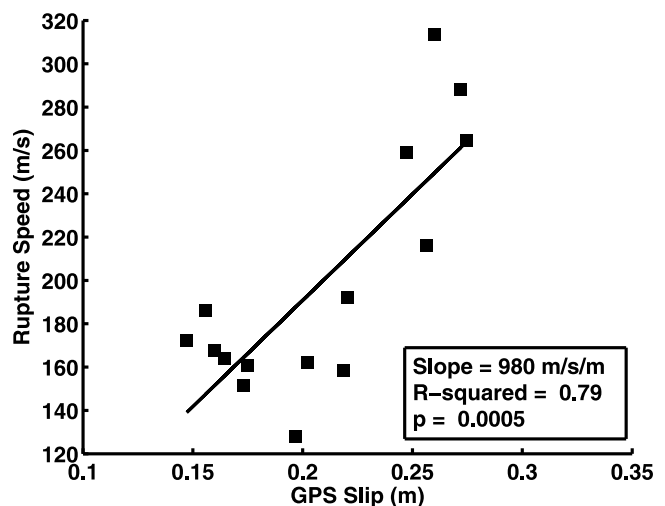


Figure 6. Rupture speed as inferred from the far-field records using equation (1) and GPS slip measured at station Whigh (see Figure 1 for station locations).

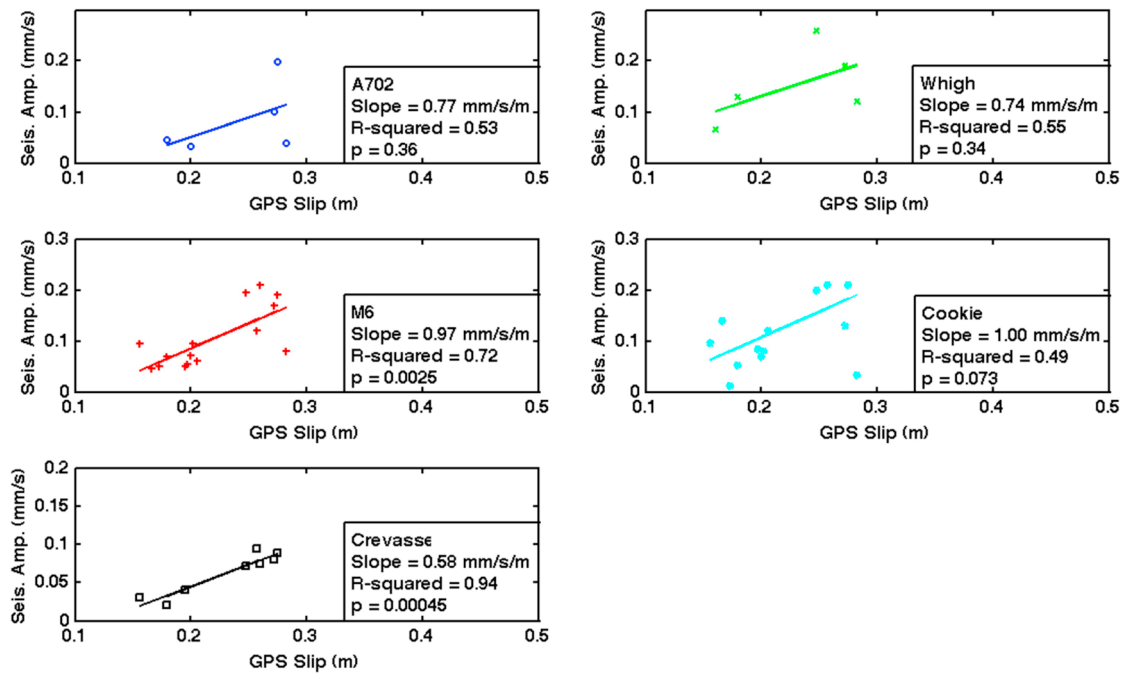


Figure 7. Slip displacement versus amplitudes of the seismic initiation for various stations in our network. The p value is the probability of the data being uncorrelated. All stations show a strong correlation. Values for slip displacement come from a single GPS station (M8) and represent the average slip for the WIP.

within 20–30 km of the nucleation zone and decreases to ~100 m/s at the edges of WIP. Given these approximate guidelines, we performed a second inversion using a velocity of 1000 m/s at the source that linearly decreases over 100 km to 0 m/s. The details of this second inversion are provided in the auxiliary material. With this second inversion, the general location of the slip start locations (Figure S1 in Text S1 of the auxiliary material) does not change significantly and all locations fall within the region shown on Figure 1, inclusive of the error ellipses.

[26] A few events are particularly diagnostic of the slip start location. For Events 19 and 20, the initiation phase arrives at station M6 prior to Whigh, and both arrivals occur within ~10 s. (see Text S2; record sections for events 19 and 20). As can be seen from the map in Figure 1, the initiation phase could not possibly arrive at M6 first, if the slip start was at ice raft A. Furthermore, if the slip events began at ice raft A, the arrivals would be separated by at least 100 s with the rupture front passing Whigh first.

3.4. Correlation of Initiation Phase Amplitude and Final Slip

[27] In order to understand the rupture process, we compare the amplitude of the initiation phase with the total slip of the event. Total slip displacement over the 20–30 min duration of each slip event is well constrained by the GPS record. Figure 7 shows the east component amplitude of the initiation phase (east axis is parallel to ice flow direction) versus GPS slip displacement at one particular GPS station, M8. We measure the amplitude of the initiation phase after applying a high-pass filter at 3000 s (Figure 2). There is a

strong linear correlation between amplitude and slip for all stations. The correlations (Figure 7 for R^2 , p value, and slope of each fit) imply that the events are slip predictable, with the probability of random occurrence (p value) being less than 1% at stations M6, Cookie, and Crevasse.

[28] Seismic waves can be generated during both acceleration and deceleration of slip and their amplitude scales with the moment rate [Lay and Wallace, 1995]. Figure 8 shows the relationship between the stopping phase B amplitude

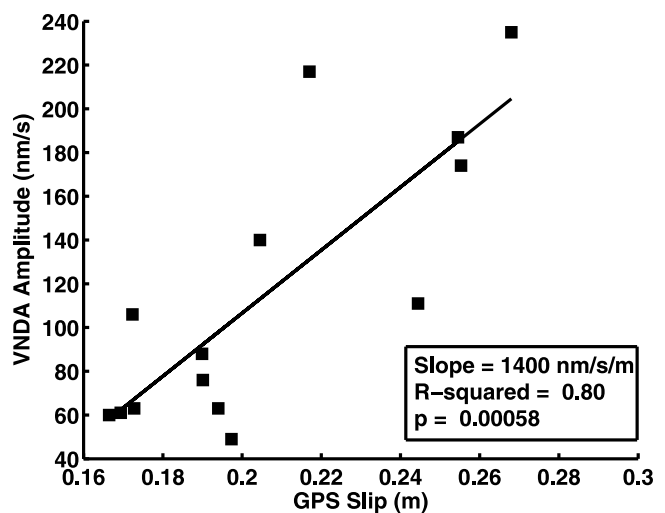


Figure 8. Far-field phase B amplitude measured at broadband station VNDA and GPS slip.

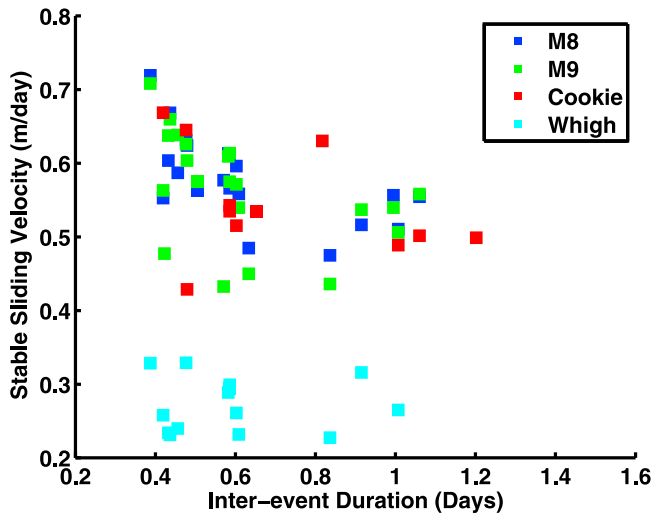


Figure 9. Measured interevent stable sliding velocity based on GPS data versus interevent duration.

and slip. The linear relationship in Figure 8 suggests that the slip events appear to stop at a rate that scales with total event slip.

3.5. Interevent Stable Sliding

[29] The WIP does not remain locked during interevent periods [Bindschadler *et al.*, 2003b]. We observe interevent surface displacement that accounts for $\sim 50\%$ of the total daily motion for most stations within our network. Given the low driving stresses of a few kPa acting on WIP, contribution of internal ice deformation to surface velocity is minor [Joughin *et al.*, 2002, 2004]. Hence, during the interevent period, the WIP is stably sliding. We calculate the average stable sliding velocity by differencing positions after a slip event and prior to the subsequent event and dividing by the elapsed time (interevent duration).

[30] We observe that the average stable sliding velocity varies for different interevent periods with the largest scatter at the smaller periods (Figure 9). For interevent periods greater than the semidiurnal period (~ 0.5 day), the interevent velocity is on average ~ 0.5 m/day for stations M8, M9, and Cookie. Station Whigh has an interevent stable sliding velocity $\sim 1/2$ that of the above three stations, yet slips nearly twice as much as M8 and M9 during slip events (Table S2 in Text S1 of the auxiliary material). Therefore the long-term average surface velocity is similar for all the stations despite the differences in partitioning of the total motion between stable sliding and slip events. This behavior suggests that there are multiple frictional asperities at the base of the WIP detectable only through measurement techniques with subdaily sampling (e.g., continuous GPS).

4. Interpretation

4.1. Comparison to Tectonic Earthquakes

[31] Glacier stick-slip motion on the WIP is a useful analogue for and may provide insight into tectonic earthquakes. The events we describe in this paper are not quite stick-slip motion, in the sense that the base is not “stuck.” Stable interevent sliding is punctuated by the arrival of a

rupture front, which initiates the unstable slip motion. Such a process is analogous to the rupture of large earthquakes into areas less coupled than the frictional asperities believed to be the predominant zones of nucleation [e.g., *Moreno et al.*, 2010]. Bidaily repeatability and relatively large rupture area on the WIP provide a rich data set for studying variations in rupture processes and assessing the balance of elastic stresses during rupture. In this paper, we have attempted to measure relevant characteristics of the rupture process, including the amplitude of a wave traveling with the rupture front propagation, slip during the event, and rupture speed of the propagation.

[32] The geometry of the glacier results in unusually close near-field records for a slip event. Most large earthquakes only intersect the surface in a relatively narrow zone and often this area is underwater at subduction zones. There is seldom an opportunity to place seismometers within 1–2 km of the rupture plane in multiple locations. Therefore, few near-source records exist that accurately record seismic wave amplitudes associated with the propagation of a rupture front. Our observations of the initiation phase amplitude scaling with eventual slip could motivate future investigations into earthquake rupture.

[33] In general, earthquake rupture speeds are usually approximately 0.9 times the shear wave speed and vary relatively little except for a few extreme cases [Kanamori and Brodsky, 2004]. There is no evidence for systematic variation of rupture speed with earthquake size. This consistency for earthquakes is thought to reflect the control of the shear wave speed on the rupture of a dynamic shear crack. Here, we have shown that rupture speeds vary by a factor of two for the WIP events and there is a systematic variation with total slip (Figure 6). In order to accommodate this difference, either the rupture propagation process must be fundamentally different than rapid shear failure observed on tectonic faults, or the shear wave velocity at the base must vary in time.

4.2. Physical Controls on Slip Start Location

[34] Our locations show that the slip starts in a region adjacent to the southern section of the WIP grounding line (Figure 1). Due to the overlapping error ellipses, we cannot assess whether the events nucleate in a critical slipping region or if there is a separate origin for each event. The location of the slip start differs significantly from a previous study [Wiens *et al.*, 2008] that located the slip starts at ice raft A and suggested that ice raft A acts as an asperity.

[35] The spatial difference between locations in our experiment and the TIDES experiment [Wiens *et al.*, 2008] could be due to migration of the dominant asperity over the 4 year period separating the experiments. Temporal variation in asperity location might be related to the century-scale slow-down of the WIS [Bougamont *et al.*, 2003], which likely causes a redistribution of the basal stresses. The WIS also contains a dynamic subglacial lake network at its base [Fricker *et al.*, 2007], which could cause stress redistribution at relatively short time scales. An elevation change anomaly designated as Lake 10 [Fricker and Scambos, 2009], which is located at the up-ice edge of the ice raft A, has been filling since observations with IceSAT began (~ 2004) and is a potential cause for the slip start migration.

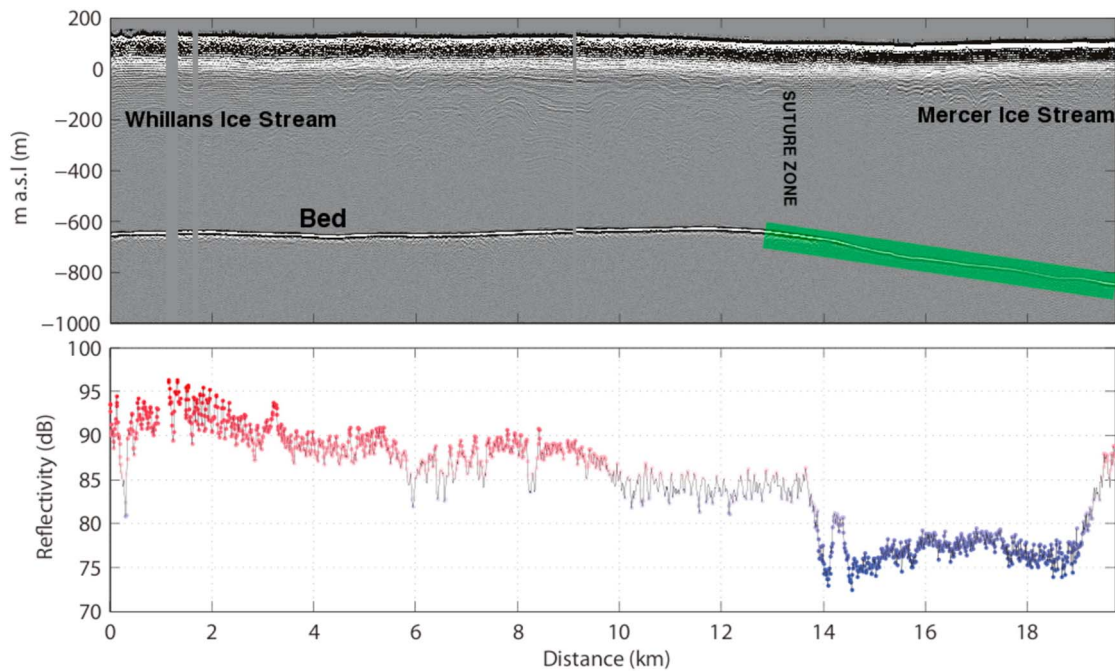


Figure 10. Ice-penetrating radar line collected across a transect from stations M6–M8, continuing southwest. Ice flow direction is directly toward the reader. (top) The green bar indicates the inferred source of slip start locations. (bottom) Red indicates high reflectivity, and blue indicates low reflectivity. Brighter reflectivity (red) typically indicates the presence of conductive pore water [Raymond *et al.*, 2006].

[36] Radar imaging of the suture helps to shed light on the basal conditions that may control the slip start location. We assume that the radar image shown in Figure 10 is representative of the suture zone in the slip start region, though it was collected ~50 km from the slip start locations. The data in Figure 10 shows that the bed is more reflective below WIS-sourced ice than MIS-sourced ice, and the height of the overlying ice increases to the southwest, which is where our origin locations cluster. Radar reflectivity of the bed is influenced by the permittivity contrast between the basal ice and the underlying geologic materials. Glaciological interpretations typically attribute a strong bed reflection to subglacial zone with abundant water and/or water that is highly conductive [e.g., Raymond *et al.*, 2006]. Weaker bed reflection is taken to indicate subglacial materials that contain less water and/or water that is less conductive. A plausible glaciological interpretation of the observed ‘dimmer’ bed south of the suture zone is that ice there is overriding bedrock, or a relatively more competent till layer than in the area to the north of the suture zone. This suggests that the slip start region is better frictionally coupled than the bed beneath the main part of the WIP. The enhanced frictional locking may allow sufficient stress to accumulate to nucleate slip events.

[37] Phase A is observed in only 5 of 26 events and its arrival time indicates that it is associated with the slip start. During our experiment, 4 of 5 phase A arrivals occur after short interevent periods, but high interevent stable sliding velocities (Figure 9). If increased stable sliding velocity translates to better coupling, then we speculate that the presence of phase A arrivals is dependent upon the degree of ice/till coupling. However, future observations will provide

better insight into the physical constraints for phase A transmission.

4.3. Initiation Phase Predicts Final Slip

[38] Figure 7 suggests that the eventual slip of the Ice Plain scales with the amplitude of the initiation phase observed at the rupture front. While amplitude is variable for each station for any given event, the relative size of the initiation phase at a single station correlates with the final GPS slip of the event. This observation implies that the magnitude of the slip event is deterministic based on the conditions during the first 30–100 s of slip.

[39] This ice slip event behavior is in contrast with tectonic earthquakes where the connection between the initiation and the final size of an earthquake is subtle enough to remain controversial [Rydelek and Horiuchi, 2006]. The slip-predictable behavior is consistent with an isolated stick-slip patch with relatively simple driving conditions. An isolated patch is expected to have regular, deterministic motion as opposed to the chaotic behavior of strongly coupled patches [Burrige and Halliday, 1971]. The stick-slip section of the WIP appears to be poised in a transitional basal regime surrounded by a combination of steady sliding and fixed boundaries.

4.4. Stress Drops for Glacier Stick-Slip Events

[40] One window into the glacial dynamics is the stress drop during slip events. Stress drops are commonly measured for earthquakes, but because the WIP is a planar slab of ice with a high length-to-thickness aspect ratio, we need to modify the standard seismological theory for this case.

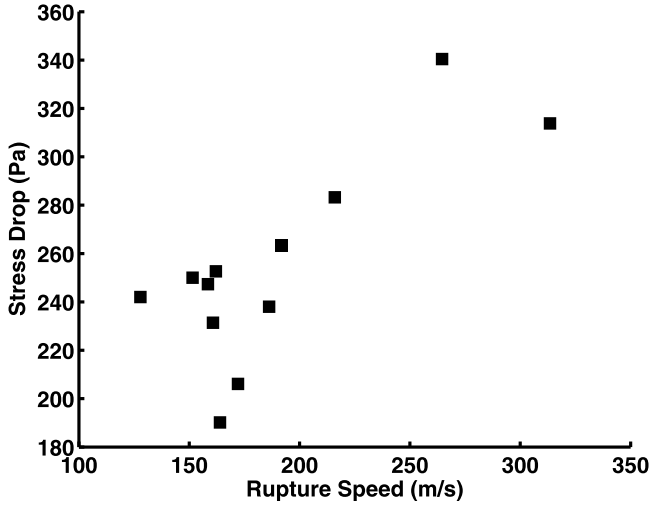


Figure 11. Stress drop plotted as inferred from the GPS slip of Figure 6 and rupture speed. Measurements of GPS slip come from station Whigh.

[41] First, we consider the stress equilibrium, $\nabla \cdot \tau = 0$, and assume that the derivatives in the y direction, perpendicular to ice flow, are negligible:

$$\frac{\partial \tau_{xz}}{\partial z} = \frac{\partial \tau_{xx}}{\partial x} \text{ or } \Delta \tau_{xz} = \frac{H}{L} \Delta \tau_{xx}, \quad (2)$$

where H is the thickness of the ice stream (~ 600 m), L is length (~ 100 km), x is the slip direction, and z is depth. Next, we use Hooke's Law for the stress-strain relationship,

$$\Delta \tau_{xx} \sim \frac{d}{L} E, \quad (3)$$

where E is Young's modulus (~ 10 GPa for ice) and d is slip. Combining equations (2) and (3), the shear stress drop, $\Delta \sigma$, is

$$\Delta \sigma = \Delta \tau_{xz} = C \frac{dH}{L^2} E, \quad (4)$$

where C is a constant of proportionality.

[42] Equation (4) is similar to one proposed and used in modeling efforts [Bindschadler *et al.*, 2003a; Winberry *et al.*, 2009] to approximate driving stresses up-ice in between stick-slip events. It differs from the usual tectonic earthquake stress drop by a factor of H/L . The constant C is typically of order one and depends on geometry [Lay and Wallace, 1995]. Since the shape of the slipping patch is largely unconstrained, we use equation (4) in its simplest form with $C = 1$ to measure the relative stress drop for each slip event. The resultant stresses range from 50 to 300 Pa and appear on Figure 11 plotted against rupture speed.

[43] In the calculations for Figure 11, we have assumed a constant rupture length. Due to the geometry of our network, we cannot directly determine rupture length of the events, but previous studies suggest that the entire WIP ruptures during events [Wiens *et al.*, 2008] and our ob-

servations in section 3.2 also favor little variation in length. If this is the case, then the stress drops vary by a factor of two for the glacial events and the variation in total seismic moment is controlled by displacement, not rupture length. This is in contrast to most earthquakes where rupture length varies in proportion to displacement [Kanamori and Anderson, 1975], with only rare exceptions in places with well-separated stick-slip patches [Harrington and Brodsky, 2009].

[44] We are hesitant to suggest that Figure 11 exhibits a linear correlation between stress drop and rupture speed, given our assumption of a constant rupture length. However, given the covariation of other observables such as rupture velocity and initiation phase amplitude with the slip, a variation of actual stress with event size could be a plausible relationship for the glacial slip events. However, this bears further investigation with future deployments of more dense instrumental arrays that can capture directly both L and d .

4.5. Interevent Basal Freezing

[45] The variation in rupture speed with slip suggests a significant variation in material properties at the base of the glacier over time. For tectonic earthquakes, the rupture velocity is limited by the shear wave velocity of the rock and is typically approximately 0.9 times the shear wave speed [Kanamori and Brodsky, 2004]. Blankenship *et al.* [1987] reported a shear wave speed for in situ till of approximately 170 m/s at a location 300 km away from our field area. We calculate rupture velocities for the WIP in the range 100–300 m/s for our idealized geometry and Wiens *et al.* [2008] report rupture velocity variations within a similar range (0.1–0.2 km/s). Even though our observations of rupture speed exceed measurements of till shear wave speed [Blankenship *et al.*, 1987] by nearly a factor of two, crack propagation is governed by the elastic properties over a broader thickness than just the till layer. Earthquake crack simulations indicate that the appropriate thickness length scale is comparable to the seismic wavelength [Harris and Day, 1997], which would be inclusive of basal ice and underlying marine sediments.

[46] The rupture speed variations suggest variations in the material properties between events, i.e., healing. Some further constraints on such a healing process are (1) WIP undergoes stick-slip events usually twice daily, which is evidence for a relatively fast healing process, (2) the correlation between rupture speed and interevent duration on Figure 12 implies time-dependent healing, and (3) the rerupture of the same large region ($\sim 100 \times 100$ km) requires that the healing process must also be pervasive. Also, if the healing process is driven by hydrological changes within the subglacial till layer (e.g., decrease in pore water pressure and associated sediment strengthening in response to basal freezing), the short repeat interval of the slip events implies that the active process zone in which healing is taking place is relatively thin. The characteristic diffusive thickness of such a zone is just several centimeters, given the low hydraulic diffusivity of West Antarctic tills of $\sim 10^{-8}$ m²/s [Tulaczyk *et al.*, 2001] and ~ 0.5 day repeat interval [Tulaczyk *et al.*, 2000a, p. 475].

[47] To explain the correlation between increased tidal loading and interevent duration, Winberry *et al.* [2009] suggested freezing as the likely interevent healing process.

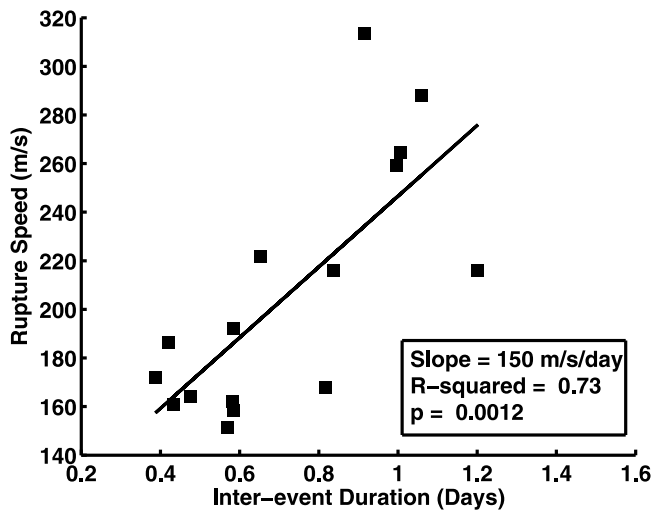


Figure 12. Rupture speed as inferred from the far-field records and interevent duration.

In order to evaluate the likelihood of such a process, we calculate the basal freezing expected during the observed interevent durations and compare it with the corresponding rupture velocities.

[48] We modify an equation from *Paterson* [1994] for the dependence of basal melting/freezing on a basal heat budget to calculate the freezing rate. We change the sign of the equation so that freezing is positive:

$$f_r = \frac{-G - \tau_b u_b + k_i \Theta_b}{L_i \rho_i}, \quad (5)$$

where f_r is freeze rate, G is the geothermal gradient, τ_b and u_b are basal shear stress and velocity, k_i is thermal conductivity of ice, Θ_b is the basal temperature gradient, L_i is latent heat of fusion, and ρ_i is the density of ice. In assigning values for the above constants, we follow previous

assumptions for the area [*Tulaczyk et al.*, 2000b; *Joughin et al.*, 2002], and use $G = 0.07 \text{ W/m}^2$, $k_i = 2.1 \text{ W/m}^\circ\text{C}$, $\Theta_b = 0.046^\circ\text{C/m}$, $L_i = 333 \text{ kJ/kg}$, and $\rho_i = 917 \text{ kg/m}^3$. We use our observed values of interevent stable sliding at station M8 for values of u_b . For basal shear stress, we input a constant value of 1 kPa, as previous work suggests a value of $1.1 \pm 0.9 \text{ kPa}$ [*Joughin et al.*, 2002]. We calculate freeze rate, f_r , and multiply by the interevent duration to obtain an estimate of the frozen thickness, where positive values represent freezing.

[49] Figure 13 shows the linear relationship between the calculated interevent basal freezing and observed rupture speed. Such a linear relationship could have been anticipated by the correlation between interevent time and rupture velocity. However, the calculation extends the observation by providing a specific physical process for the correlation, which has implications for other observables within equation (5).

[50] The freeze rate calculation (equation (5)) is highly sensitive to the product of $\tau_b u_b$. For the basal shear stress, τ_b , we used the nominal value of 1 kPa, based on *Joughin et al.* [2002]. In order to assess the sensitivity of our results to this assumption and to place a maximum constraint on basal shear stress, we varied the basal shear stress and calculated the associated freezing, using the range of values for u_b from GPS station M8. Figure 14 shows the associated freezing expected based on equation (5), when the basal shear stress is allowed to vary between 0 and 5 kPa. The basal interface transitions into melting near the value of 4 kPa for the range of velocities we observe at our stations.

[51] A further constraint on the basal processes comes from the long-term behavior of WIS. *Joughin et al.* [2004] shows that the annually averaged velocities for the WIS have been decreasing over the last few decades and suggested basal freezing as the primary mechanism for such a slow-down. Numerical models suggest a similar mechanism for shutdown [*Bougamont et al.*, 2003] of WIS. Recent slider block models of glacier friction suggest that stick-slip

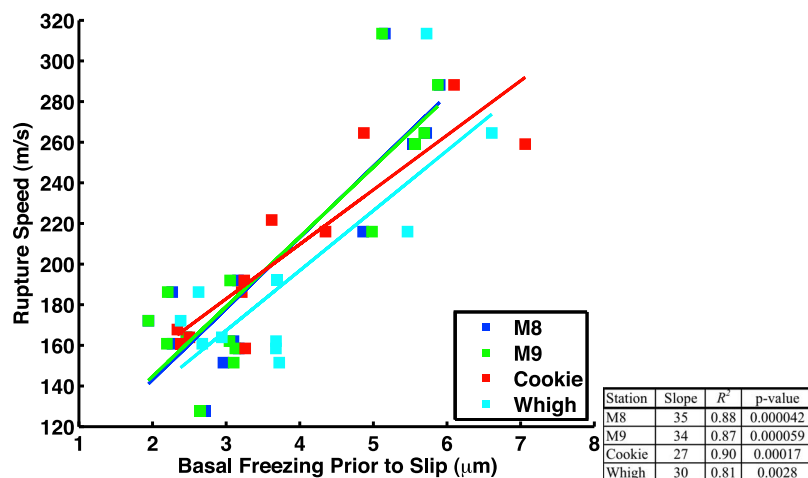


Figure 13. Basal freeze-on calculated from equation (5) and the GPS data from Figure 9 and rupture velocity for the resultant slip event, inferred from far-field stations. Basal freeze-on is calculated over the duration of interevent time leading up to the slip event.

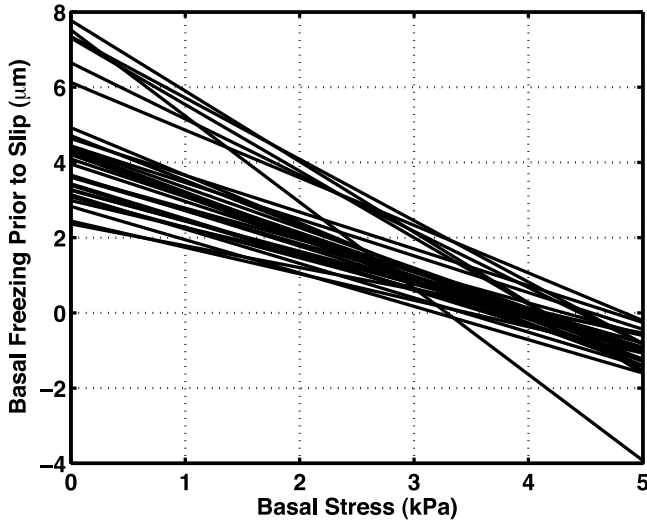


Figure 14. Freezing for a range of interevent basal shear stress τ_b in equation (5). This calculation is used to constrain the range of basal shear stresses that are realistic, and as freezing must be positive over the long-term, τ_b must be less than 4 kPa based on the range of velocities we observe. We use observed interevent velocity, u_b , from station M8.

behavior, which is now observed on the WIP, is a transitional response to decreasing velocity or increasing static friction, such as would accompany freezing [Sergienko *et al.*, 2009].

[52] Based on our observations of the range of interevent sliding velocities, and in order to obtain net freezing over long time periods in equation (5), the basal shear stress is constrained to be below the 4 kPa value. During unstable sliding (slip event), the basal velocity (~ 0.5 m over ~ 30 min is ~ 24 m/day) is at least an order of magnitude faster than during interevent stable sliding (Figure 9) and promotes melting, therefore the shear stress must be significantly below this upper bound.

[53] In summary, we have shown that at its current surface velocity, the WIP promotes basal freezing, at subdaily time scales, up to a limit of 4 kPa, where it transitions to promoting melting. Our results suggest interevent freezing at a maximum of 7 microns. The freezing can increase the static friction at the base. It can also affect shear wave velocities, and hence rupture velocities, as elastic properties can be very sensitive to grain boundary fluids [Takei, 1998].

[54] Direct measurements do not exist of such small magnitude basal freezing, nor would such a small change be easily directly detected between subsequent slip events. Yet, freezing of this magnitude may be important for glacier dynamics, as laboratory ring shear experiments of glacier till indicate that strain within till is confined to relatively narrow zones [Iverson *et al.*, 1998].

5. Summary and Conclusions

[55] We present new near-field data for glacial slip events collected during the austral summer of 2008. We observe that the slip events contain a distinct initiation phase only observable in the near field. The amplitude of the initiation

phase increases with final slip and rupture velocities, indicating that both of these quantities are determined from the start of rupture. The ruptures begin in a region near the suture zone between Whillans and Mercer Ice Streams. Radar data indicates a distinction in bed properties that is consistent with the slip events nucleating in a relatively drier, higher-friction region. Between events, the rupture region continues to stably slide at a lower rate indicating incomplete locking with the base.

[56] The variation of slip between events and slip predictability are consistent with standard stick-slip models of earthquakes on isolated asperities. However, the variation in rupture velocity with size is a distinct feature of glacial events that may be explained by a variation in shear wave velocities controlled by extremely small-scale interevent freezing. In order for this freezing to occur, the basal shear stress cannot exceed 4 kPa.

Appendix A: Slip Start Location Inversion

[57] We implement a 2-D (x, y, t) iterative linear least squares inversion to locate the slip event start location [Stein and Wysession, 2003]. We use seismic initiation phase arrival times at each of the on-ice stations as the data vector \underline{d} . In our case, \underline{d} is an $n \times 1$ vector, where n is the number of observing stations for that particular event.

[58] Given an initial guess of origin location and time, we form the model vector $\underline{m} = (x, y, t)$. We then calculate the predicted arrival time vector \underline{d}' at each station in the data set using the rupture velocity particular to each event from Table S2 in Text S1 of the auxiliary material, station locations and the model vector \underline{m} . Travel time from the basal layer, through the ice, is neglected. The residual between the predicted arrival time and the observations is $\Delta \underline{d} = \underline{d}' - \underline{d}$. The model vector is then improved by determining the derivatives of the arrival times predictions with respect to the model parameters. We define the components of the $n \times 3$ matrix \underline{G} by $G_{ij} = \frac{\partial d_i}{\partial m_j}$ and the requisite model increment is related to the residual by $\Delta \underline{d} = \underline{G} \Delta \underline{m}$. The least square solution for the model increment is $\Delta \underline{m} = (\underline{G}^T \underline{G})^{-1} \underline{G}^T \Delta \underline{d}$. We perform 10 iterations of the inversion, adding successive values of $\Delta \underline{m}$ to the previous iteration of \underline{m} , to obtain an origin location and time.

[59] The standard deviations for the model vector are determined by $\sigma_m^2 = \sigma^2 (\underline{G}^T \underline{G})^{-1}$ [Stein and Wysession, 2003, section 7.2, equation 34], where σ is the standard deviation of the residual vector $\Delta \underline{d}$. Two standard deviations define the 95% confidence interval and are used to define the semimajor axes of the ellipses on Figure 1.

[60] **Acknowledgments.** Thorough and thoughtful reviews by the Associate Editor, Martin Truffer, Fabian Walter, and Paul Winberry considerably improved this paper. This work was funded primarily by NSF Antarctic Sciences Division grant 0636970. A NASA Earth and Space Science Fellowship provided support for J.I.W. We would like to thank John Woodward and Saffia Hossainzadeh for assistance in the field. We thank Dan Sampson for providing technical assistance prior to fieldwork and Doug Wiens for loaning some of the passive seismic sensors. Raytheon Polar Services provided field support and logistics. The GPS stations were provided by the UNAVCO Facility with support from the National Science Foundation and NASA under NSF Cooperative Agreement EAR-0735156. Some of the instruments used in the field program were provided by the PASSCAL facility of the Incorporated Research Institutions for Seismology (IRIS) through the PASSCAL Instrument Center at New Mexico Tech. Data collected during this experiment will

be available through the IRIS Data Management Center. The facilities of the IRIS Consortium are supported by the National Science Foundation under Cooperative Agreement EAR-0552316 and by the Department of Energy National Nuclear Security Administration.

References

- Bindschadler, R. A., M. A. King, R. B. Alley, S. Anandakrishnan, and L. Padman (2003a), Tidally controlled stick-slip discharge of a West Antarctic ice stream, *Science*, *301*, 1087–1089, doi:10.1126/science.1087231.
- Bindschadler, R. A., P. L. Vornberger, M. A. King, and L. Padman (2003b), Tidally driven stick-slip motion in the mouth of Whillans Ice Stream, *Ann. Glaciol.*, *36*, 263–272, doi:10.3189/172756403781816284.
- Blankenship, D. D., S. Anandakrishnan, J. L. Kempf, and C. R. Bentley (1987), Microearthquakes under and alongside Ice Stream B, Antarctica, *Ann. Glaciol.*, *9*, 30–34.
- Bougamont, M., S. Tulaczyk, and I. Joughin (2003), Numerical investigations of the slow-down of Whillans Ice Stream, West Antarctica: Is it shutting down like Ice Stream C?, *Ann. Glaciol.*, *37*, 239–246, doi:10.3189/172756403781815555.
- Brace, W. F., and J. D. Byerlee (1966), Stick-slip as a mechanism for earthquakes, *Science*, *153*, 990–992, doi:10.1126/science.153.3739.990.
- BurrIDGE, R., and G. S. Halliday (1971), Dynamic shear cracks with friction as models for shallow focus earthquakes, *Geophys. J. R. Astron. Soc.*, *25*, 1–3.
- FrickeR, H. A., and T. Scambos (2009), Connected subglacial lake activity on lower Mercer and Whillans Ice Streams, West Antarctica: 2003–2008, *J. Glaciol.*, *55*(190), 303–315, doi:10.3189/002214309788608813.
- FrickeR, H. A., T. Scambos, and R. Bindschadler (2007), An active subglacial water system in West Antarctica mapped from space, *Science*, *315*, 1544–1548, doi:10.1126/science.1136897.
- Gades, A. M., C. F. Raymond, H. Conway, and R. W. Jacobel (2000), Bed properties of Siple Dome and adjacent ice streams, West Antarctica, inferred from radio-echo sounding measurements, *J. Glaciol.*, *46*(152), 88–94, doi:10.3189/172756500781833467.
- Harrington, R. M., and E. E. Brodsky (2009), Source duration scales with magnitude differently for earthquakes on the San Andreas Fault and on secondary faults in Parkfield, California, *Bull. Seismol. Soc. Am.*, *99*, 2323–2334.
- Harris, R. A., and S. M. Day (1997), Effects of a low-velocity zone on a dynamic rupture, *Bull. Seismol. Soc. Am.*, *87*, 1267–1280.
- Horgan, H. J., and S. Anandakrishnan (2006), Static grounding lines and dynamic ice streams: Evidence from the Siple Coast, West Antarctica, *Geophys. Res. Lett.*, *33*, L18502, doi:10.1029/2006GL027091.
- Iverson, N. R., T. S. Hooyer, and R. W. Baker (1998), Ring shear studies of till deformation: Coulomb plastic behavior and distributed strain in glacier beds, *J. Glaciol.*, *44*(148), 634–642.
- Jacobel, R., B. Welch, D. J. Osterhouse, R. Pettersson, and J. A. MacGregor (2009), Spatial variation of radar-derived basal conditions on Kamb Ice Stream, *Ann. Glaciol.*, *50*, 10–16, doi:10.3189/172756409789097504.
- Joughin, I., S. Tulaczyk, R. Bindschadler, and S. F. Price (2002), Changes in west Antarctic ice stream velocities: Observation and analysis, *J. Geophys. Res.*, *107*(B11), 2289, doi:10.1029/2001JB001029.
- Joughin, I., S. Tulaczyk, D. R. MacAyeal, and H. Engelhardt (2004), Melting and freezing beneath the Ross Ice Streams, Antarctica, *J. Glaciol.*, *50*(168), 96–108, doi:10.3189/172756504781830295.
- Kanamori, H., and D. L. Anderson (1975), Theoretical basis of some empirical relations in seismology, *Bull. Seismol. Soc. Am.*, *65*, 1073–1095.
- Kanamori, H., and E. E. Brodsky (2004), The physics of earthquakes, *Rep. Prog. Phys.*, *67*, 1429–1496, doi:10.1088/0034-4885/67/8/R03.
- Lay, T., and T. C. Wallace (1995), *Modern Global Seismology*, 521 pp., Academic, San Diego, Calif.
- Moreno, M., M. Rosenau, and O. Oncken (2010), 2010 Maule earthquake slip correlates with pre-seismic locking of Andean subduction zone, *Nature*, *467*, 198–202, doi:10.1038/nature09349.
- Paterson, W. S. B. (1994), *The Physics of Glaciers*, 3rd ed., 480 pp., Pergamon, Oxford, U. K.
- Raymond, C. F., G. A. Catania, N. Nereson, and C. J. Van der Veen (2006), Bed radar reflectivity across the north margin of Whillans Ice Stream, West Antarctica, and implications for margin processes, *J. Glaciol.*, *52*(176), 3–10, doi:10.3189/172756506781828890.
- Rydelek, P., and S. Horiuchi (2006), Earth Science: Is earthquake rupture deterministic?, *Nature*, *442*, E5–E6, doi:10.1038/nature04963.
- Sergienko, O. V., D. R. MacAyeal, and R. A. Bindschadler (2009), Stick-slip behavior of ice streams: Modeling investigations, *Ann. Glaciol.*, *50*, 87–94, doi:10.3189/172756409789624274.
- Shabtaie, S., I. M. Whillans, and C. R. Bentley (1987), The morphology of Ice Streams A, B, and C, West Antarctica, and their environs, *J. Geophys. Res.*, *92*, 8865–8883, doi:10.1029/JB092iB09p08865.
- Stein, S., and M. Wysession (2003), *An Introduction to Seismology: Earthquakes and Earth Structure*, Blackwell, Malden, Mass.
- Takei, Y. (1998), Constitutive mechanical relations of solid-liquid composites in terms of grain-boundary contiguity, *J. Geophys. Res.*, *103*, 18,183–18,203, doi:10.1029/98JB01489.
- Tulaczyk, S., B. Kamb, and H. Engelhardt (2000a), Basal mechanics of Ice Stream B, West Antarctica: 1. Till mechanics, *J. Geophys. Res.*, *105*, 463–481, doi:10.1029/1999JB900329.
- Tulaczyk, S., B. Kamb, and H. Engelhardt (2000b), Basal mechanics of Ice Stream B, West Antarctica: 2. Undrained plastic bed model, *J. Geophys. Res.*, *105*, 483–494, doi:10.1029/1999JB900328.
- Tulaczyk, S., B. Kamb, and H. F. Engelhardt (2001), Estimates of effective stress beneath a modern West Antarctic ice stream from till pre-consolidation and void ratio, *Boreas*, *30*, 101–114, doi:10.1080/030094801750203134.
- Wiens, D. A., S. Anandakrishnan, J. P. Winberry, and M. A. King (2008), Simultaneous teleseismic and geodetic observations of the stick-slip motion of an Antarctic ice stream, *Nature*, *453*, 770–774, doi:10.1038/nature06990.
- Winberry, J. P., S. Anandakrishnan, R. B. Alley, R. A. Bindschadler, and M. A. King (2009), Basal mechanics of ice streams: Insights from the stick-slip motion of Whillans Ice Stream, West Antarctica, *J. Geophys. Res.*, *114*, F01016, doi:10.1029/2008JF001035.
- Winebrenner, D. P., B. E. Smith, G. A. Catania, H. B. Conway, and C. F. Raymond (2003), Radio-frequency attenuation beneath Siple Dome, West Antarctica, from wide-angle and profiling radar observations, *Ann. Glaciol.*, *37*, 226–232, doi:10.3189/172756403781815483.

E. E. Brodsky, S. Y. Schwartz, S. Tulaczyk, and J. I. Walter, Department of Earth and Planetary Sciences, University of California, 1156 High St., Santa Cruz, CA 95064, USA. (brodsky@pmc.ucsc.edu; susan@pmc.ucsc.edu; tulaczyk@pmc.ucsc.edu; jwalter@ucsc.edu)

R. Pettersson, Department of Earth Sciences, Uppsala University, Villavägen 16, SE-752 36 Uppsala, Sweden. (rickard.pettersson@geo.uu.se)